

Chapter 5. Radar Interactions With Geologic Surfaces

Tom G. Farr

Introduction

The correct geologic interpretation of radar images depends critically on a knowledge of how radar waves interact with natural surfaces. There are significant differences between the microwave and more familiar optical wavelengths in the mechanics of imaging and in the measured characteristics of the target. Because of the side-looking illumination geometry, all radar images are distorted to some extent. In addition, the longer wavelength of radar waves makes them most sensitive to surface roughness at scales near the radar wavelength. Of secondary importance are variations in the dielectric constant of the target; this parameter is similar for dry geologic materials except metallic compounds, which may be present at high elevations on Venus. The geometric and electromagnetic interactions of radar waves with natural surfaces, then, must be considered for accurate interpretation of Magellan SAR images.

The Geometry of Radar Imaging

Since radars depend on the measurement of range to create an image in the cross-track direction, they are forced to look to the side to allow the sensor to differentiate between objects to the left and right of the ground track; in the along-track direction, platform motion and Doppler frequency shift create the image. Synthetic aperture and matched-filter techniques, described by Elachi [1988], are used to obtain high resolution in these directions.

This side-looking geometry has a number of descriptive terms and peculiarities that must be understood when

interpreting radar images (Figure 5-1). The angle at which the radar images the target as measured from the horizontal at the antenna is called the depression angle. The look angle, θ_l , is the complement of the depression angle. At the target, local undulations combined with the look angle create a local incidence angle, θ_i (Figure 5-1). Note that even for horizontal terrain, the look angle does not equal the local incidence angle because of planetary curvature. This effect is small for aircraft sensors but significant for spacecraft:

$$\theta_i = \arcsin\left(\frac{r+H}{r} \sin \theta_l\right)$$

where r is the radius of Venus and H is the altitude of the spacecraft.

The fact that imaging radars divide the range into small intervals to create range pixels yields a projected geometry when the slant-range pixels are written to film (Figure 5-2). A slant-range image appears compressed in the near range because of this projection. Assuming a horizontal surface, the simple transformation

$$G = H \sqrt{\frac{1}{\cos^2 \theta_i} - 1}$$

produces a ground-range image, where G is the ground-range distance. Note, however, that topographic variations are not accounted for in this transformation.

Topographic variations are distorted in the same way as the overall image: Their near-range points are compressed relative to their far-range points (Figure 5-3). The general

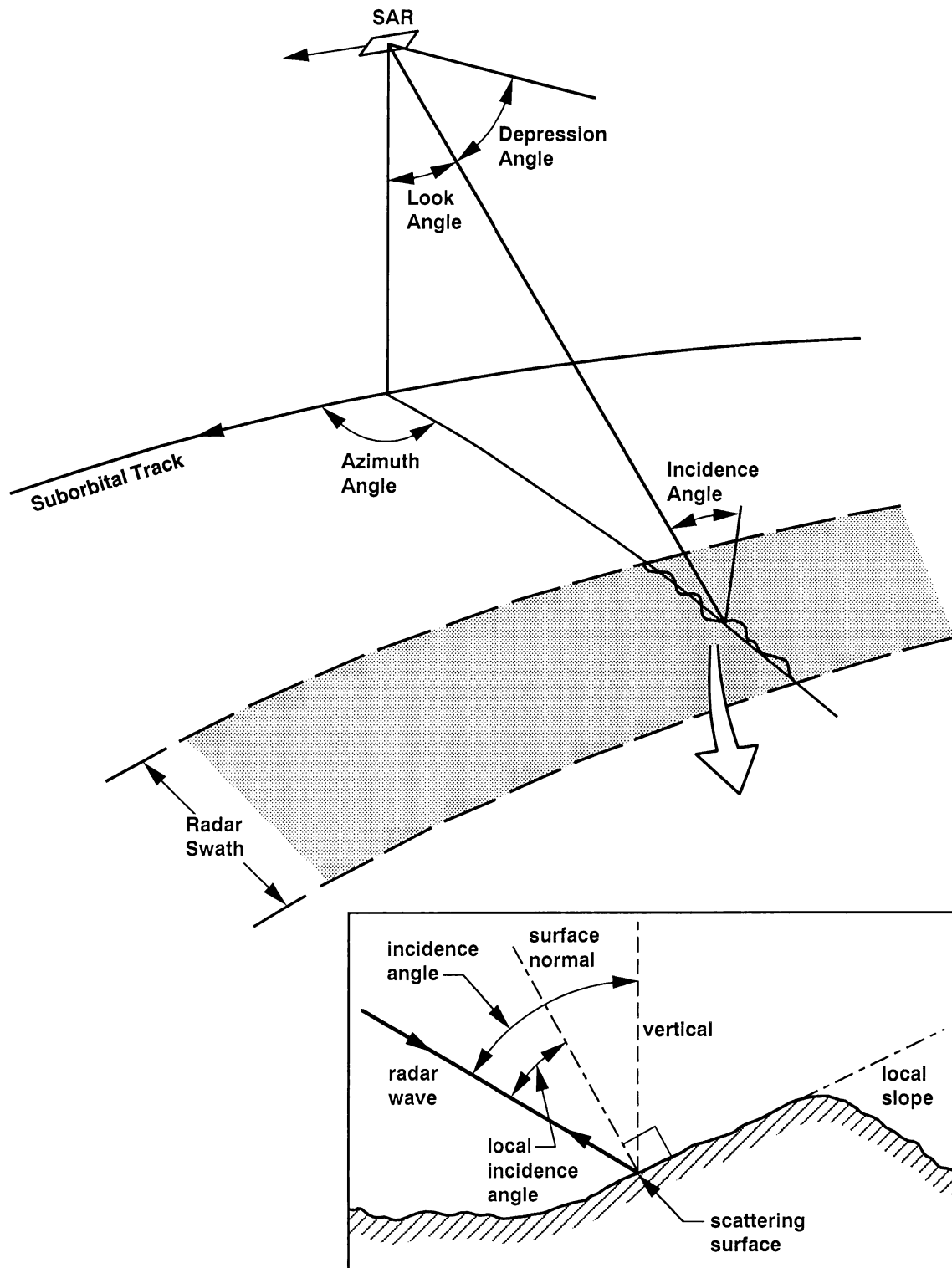


Figure 5-1. Geometry of radar image acquisition. The depression angle is complementary to the look angle; the incidence angle may be affected by planetary curvature. Local incidence angle may be affected by local topography.

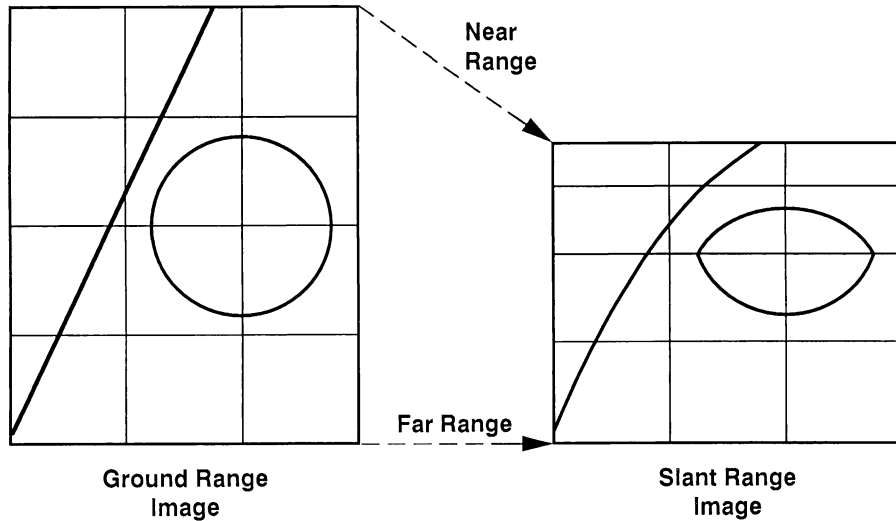
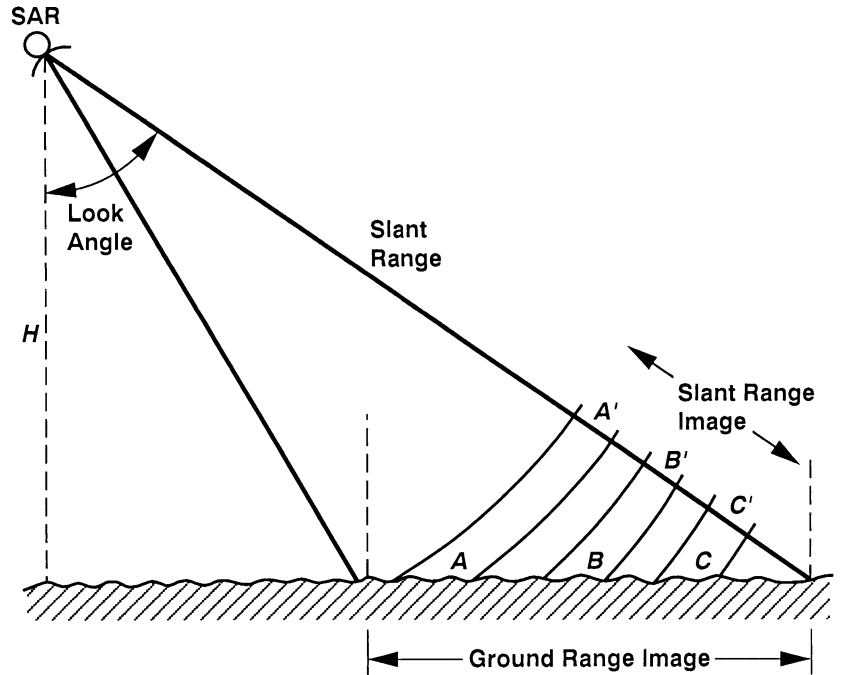
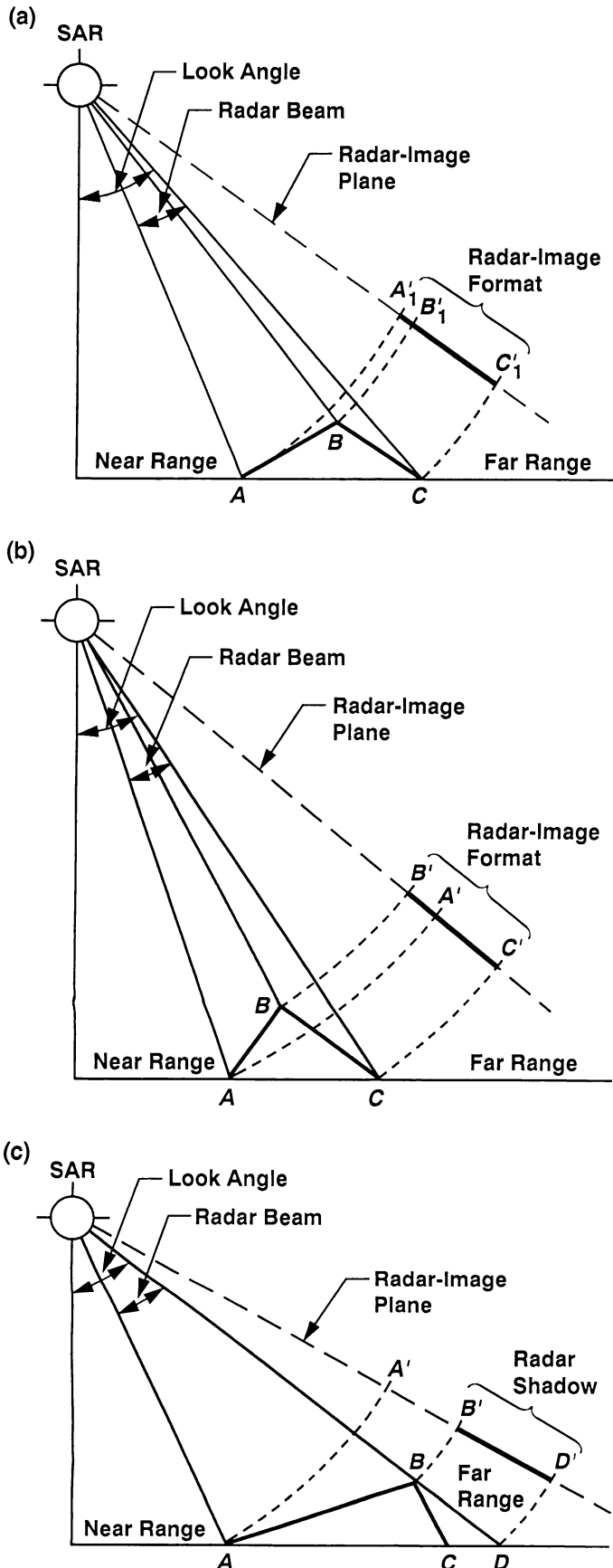


Figure 5-2. Slant-range and ground-angle geometries. Knowledge of the spacecraft height, H , and incidence angle allows correction of slant-range geometry, where targets in near range appear compressed with respect to those in far range.

case of radar foreshortening compresses the image of a mountain's near-range slope and extends the image of its back slope (Figure 5-3(a)). The effect is obviously exacerbated by small look angles and steep slopes to the extreme case of layover, in which the top of the mountain is imaged before the bottom of the near-range slope (Figure 5-3(b)). Image data in the laid-over area are lost. Image data can also be lost on the

backslope if the slope is steep enough and the look angle large enough to put the slope in radar shadow (Figure 5-3(c)). Layover and shadow can be seen in a Seasat SAR image of the Alaska Range (Figure 5-4), where the top of a mountain is superimposed on the glacier at its foot, while the backslopes of the mountains are in shadow. Seasat SAR had a look angle of about 20 deg.



As a generalization, since most slope angles on Earth are less than about 35 deg, imaging radars with small look angles, such as Seasat, enhance the topography at the expense of surface roughness information (discussed later).

Conversely, larger look angles, such as SIR-A's 47 deg, reduce the effect of topography and enhance the sensitivity to surface roughness (Figure 5-5).

These aspects of imaging radar geometry are especially important in interpreting Magellan SAR images, as the look angle varies systematically with latitude (Figure 4-3). The wide range of look angles extends beyond the range of the Seasat SAR and SIR-A angles and encompasses shallow slope angles typical of eroded terrain, through angles equal to the angle of repose of loose granular material (i.e., sand and talus), to over-steepened angles typical of tectonically active mountains. Thus, different types of relief will be accentuated depending on latitude.

The orientation of linear features relative to the radar look direction or azimuth also controls the visibility of the features (Figure 5-6). Where the illumination is *parallel* to the structure, there is little effect on the local incidence angle and therefore no enhancement of the structure. Conversely, topographic variations stand out where illumination is *normal* to the structure. Obviously, this effect is accentuated by a small look angle.

A dramatic example of another look–azimuth effect is shown in Figure 5-7, which is a pair of Magellan SAR images obtained from nearly opposite look directions at nearly the same look angle. Bright areas in the upper image, which is illuminated from the west (left), are not present in the lower image, which is illuminated from the east. A possible explanation is that asymmetric ripples or dunes are oriented approximately north–south, with local slope angles equal to the look angle on the west and much different angles on the east. Another possibility is that the surface changed, perhaps in response to wind action, in the 8-month interval between the two passes.

Roughness

Radar waves impinging on a surface scatter from the surface and near-surface volume. Very smooth surfaces at the

Figure 5-3. Geometric distortions in radar images: (a) radar image foreshortening, where the slope facing the radar is compressed to segment $A' - B'$ while the backslope is extended to segment $B' - C'$; (b) radar layover, an extreme case of foreshortening, where the top of the mountain, B' , is imaged before the bottom, A' ; (c) radar shadowing, where the backslope of the mountain, $B' - D'$, is not illuminated by the radar, and no data are acquired.

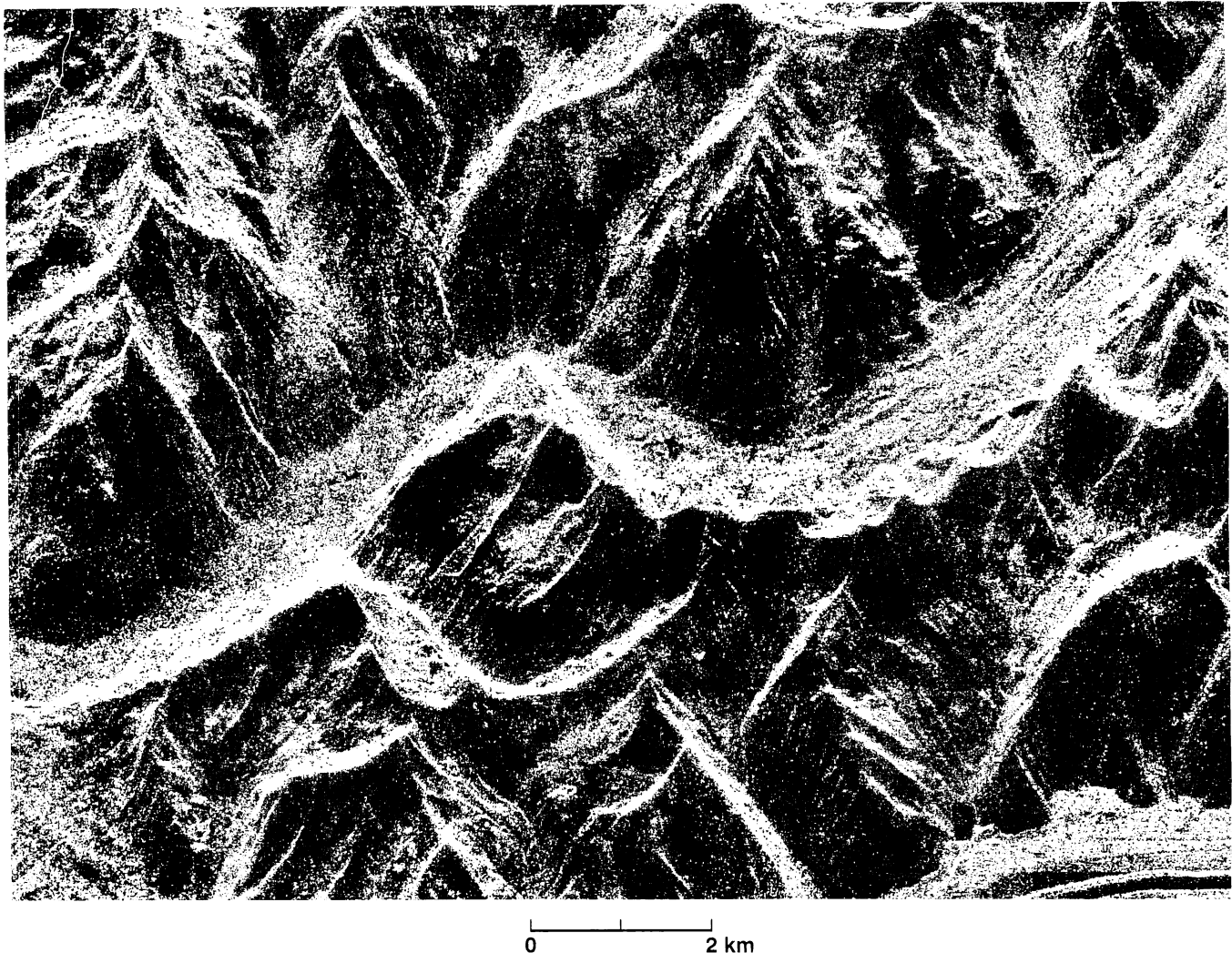


Figure 5-4. Example of radar image layover. Seasat image of the Alaska Range showing the top of a mountain imaged onto the glacier at its foot (center). Shadows are also present on many of the backslopes of these steep mountains. Illumination is from the top [from Ford et al., 1989].

scale of the radar wavelength (λ) scatter the incident radiation in the specular direction (Figure 5-8); this scattering is a mirrorlike reflection often called “specular reflection.”

Rougher surfaces cause more of the radar energy to be scattered randomly until it reaches a diffuse, Lambertian distribution. The Magellan SAR, like most imaging radars, is monostatic, i.e., the same antenna is used for transmission and reception. Comparison of the cases in Figure 5-8 shows that the smooth surface has no component of its return in the direction of the transmission arrow, so the resulting image tone would be black. With increasing roughness, more energy is scattered back to the antenna, resulting in lighter image tones for rougher surfaces.

Changes in the local incidence angle for the surfaces shown in Figure 5-8 produce characteristic curves of image brightness, quantified as radar backscatter vs. incidence angle (Figure 5-9). Clearly, a smooth surface produces a sharp peak when the radar illumination is perpendicular to it (incidence angle = 0 deg), while a very rough surface scatters the signal equally in all directions with little dependence on incidence angle. The curves in Figure 5-9 show that smooth surfaces can be brighter than rough surfaces at small incidence angles (typically less than 20 to 25 deg); these small angles are typical for the Magellan SAR data in the high latitudes of Venus. An erroneous interpretation of roughness can result if look angle is not taken into account.

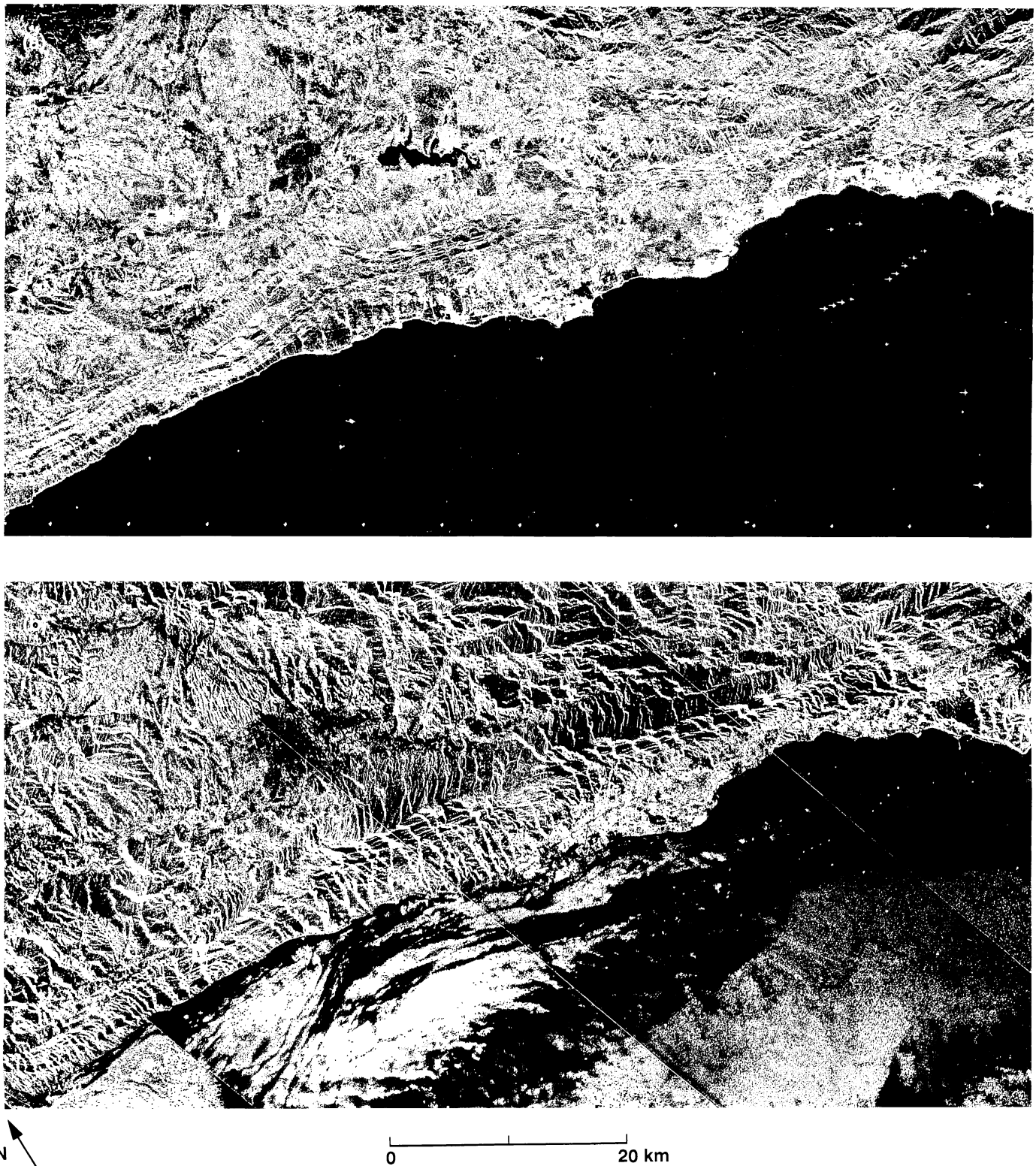


Figure 5-5. Enhancement of roughness and topography: (a) SIR-A image of the Santa Ynez Mountains in California obtained at about a 50-deg incidence angle—at this angle, surface roughness effects dominate the image; (b) Seasat image of the scene in (a) obtained at about a 20-deg incidence angle—at this small angle, topography is enhanced because the slopes are closer to this small value. Illumination is from the bottom in (a) and from the lower left corner in (b).

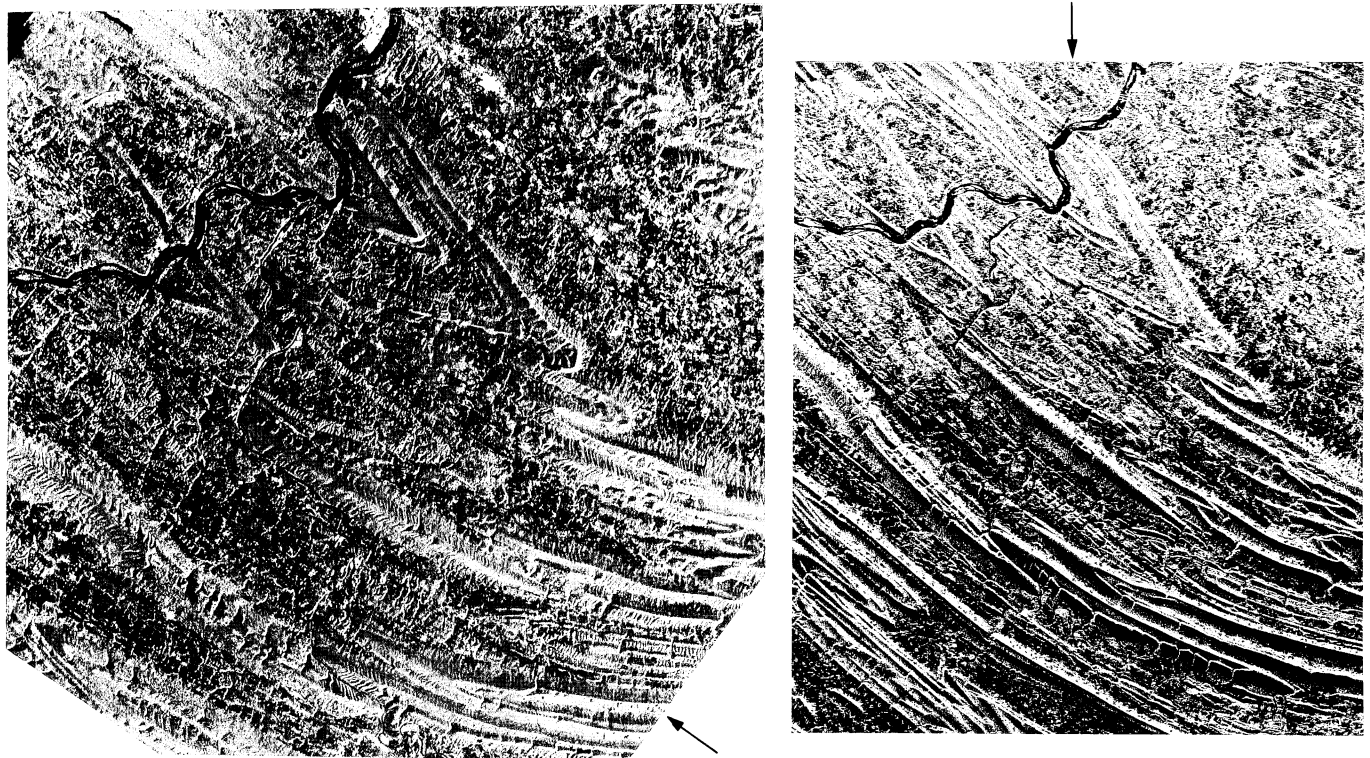


Figure 5-6. Azimuth viewing effects in radar images. Seasat observed the folded Appalachians in Pennsylvania from two directions, shown by the arrows. The structures are highlighted where illumination is nearly perpendicular to the ridges, while the contrasts in topography almost disappear where the illumination is parallel to the ridges.

The scattering behavior of radar waves from rough surfaces can be quantified through the use of scattering models that relate surface roughness to the radar backscatter [e.g., Ulaby et al., 1982; Fung and Pan, 1987; Kim et al., 1992; Rodríguez et al., 1992; Rodríguez and Kim, 1992]. However, before discussing the scattering models themselves, the quantitative description of surface roughness deserves some review.

A breakpoint between smooth and rough surfaces (and the corresponding dominant radar scattering mechanisms) is loosely implied by the Rayleigh criterion. According to this criterion, a surface is considered smooth if the root-mean-square (rms) height of the microrelief is less than one-eighth of the radar wavelength divided by the cosine of the incidence angle:

$$h < \lambda/8 \cos \theta$$

where h is the rms height, λ is the wavelength, and θ is the incidence angle. Because this criterion does not consider an intermediate category of surfaces between definitely smooth and definitely rough, it was modified by Peake and Oliver

[1971] to include factors that define the upper and lower values of rms surface smoothness or roughness. The modified Rayleigh criterion considers a surface smooth where

$$h < \lambda/25 \cos \theta$$

and rough where

$$h > \lambda/4.4 \cos \theta$$

Field measurements of different types of surfaces have led researchers to experiment with a variety of different descriptors [e.g., Schaber et al., 1976 (geologic surfaces); Ulaby et al., 1982 (agricultural surfaces)]. This illustrates one of the difficulties associated with modeling the radar behavior of natural surfaces. Regardless of the description that is used, it follows from the equations that at any incidence angle a given surface appears rougher as the wavelength decreases and, independent of wavelength, a given surface appears smoother as the incidence angle increases.

Describing the roughness of a surface by its rms height excludes any description of the scales of roughness. The scales of roughness can be described by calculating the

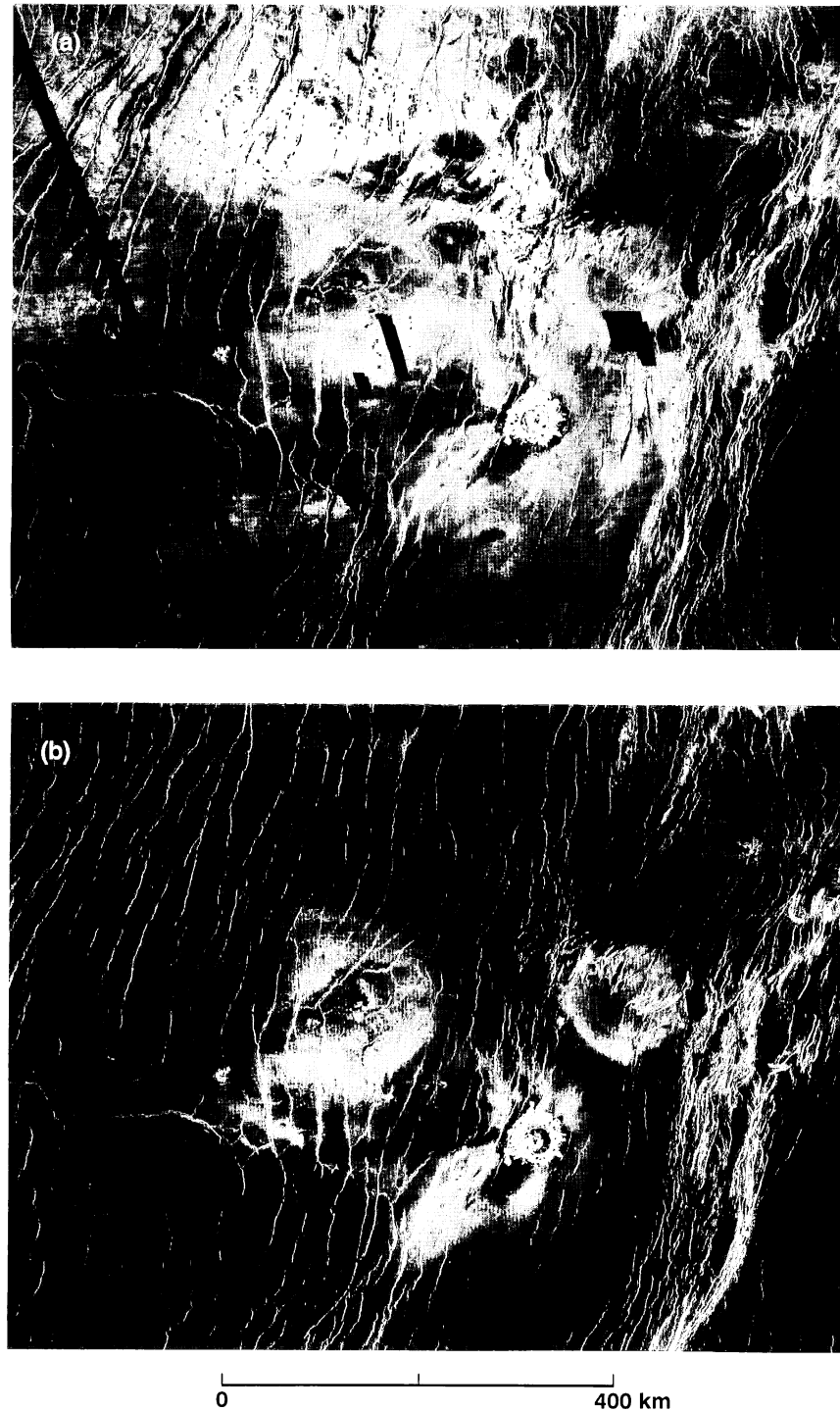


Figure 5-7. Azimuth viewing effects in Magellan SAR images of an area centered at about 58°S, 200°E in Imdr Regio: (a) obtained in February 1991 with illumination from the west (left) at an incidence angle of about 21 deg; (b) obtained in October 1991 with illumination from the east (right) at an incidence angle of about 24 deg. Many bright areas in (a) are not present in (b), which indicates (1) the surface has asymmetric roughness with slopes of about 21 deg facing west (to give the bright return) and much different slopes facing east, or (2) the surface was altered by surficial processes in the 8 months between the two images.

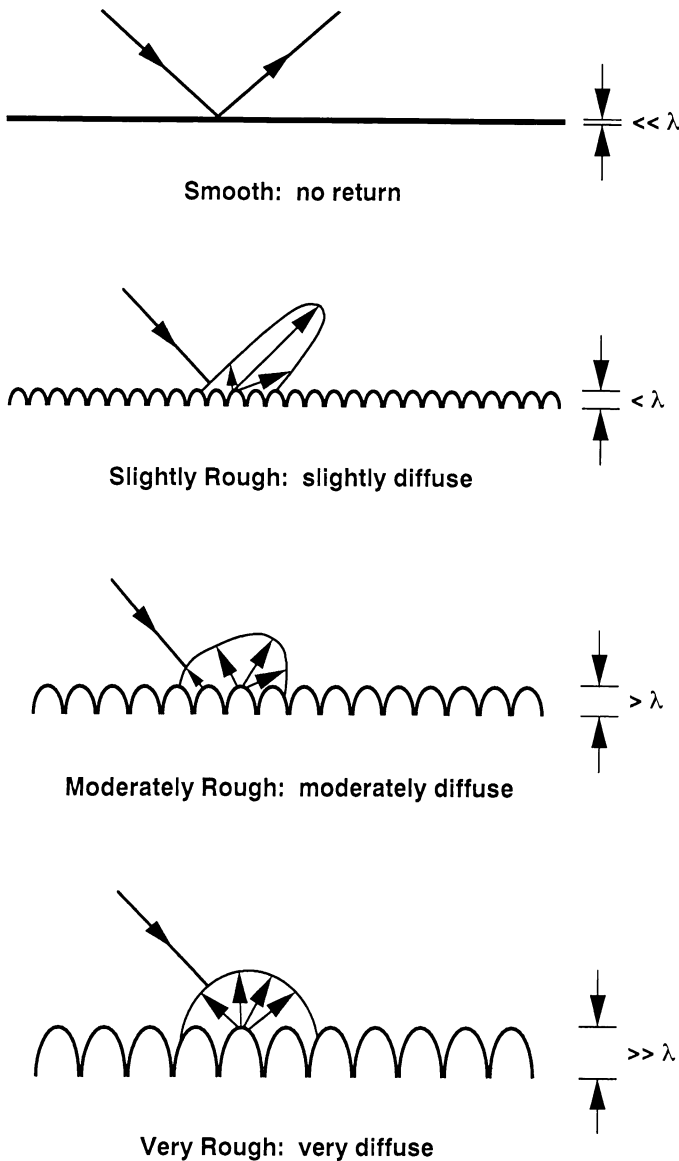


Figure 5-8. Surface roughness effects on radar backscatter. Surfaces whose roughness is much less than the radar wavelength scatter in the specular direction. Rougher surfaces scatter more energy in all directions, including the direction back to the receiving antenna.

correlation length of profiles: Correlation length is a measure of how quickly heights change along a profile. The autocorrelation function for a surface profile is calculated by sequentially stepping the profile across a stationary copy, multiplying, and normalizing. This function is unity for 0 steps, or lags, and drops as the number of lags increases. The rate of the drop-off, measured by the lag at which the autocorrelation value equals $1/e$, is called the correlation length, l . Smoother surfaces have larger correlation lengths [e.g., Ulaby et al., 1982, p. 822].

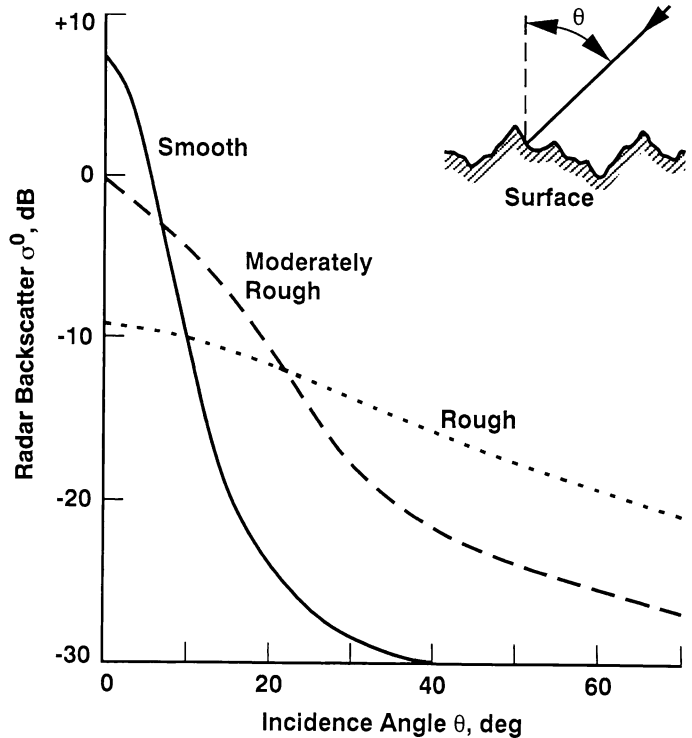


Figure 5-9. Radar backscatter as a function of incidence angle for representative surfaces. For angles less than about 25 deg, smoother surfaces have greater backscatter than rougher surfaces.

Another way to describe quantitatively both the amplitude and scale of surface roughness is through the power spectrum, or power spectral density, usually of profiles. Without going into the mathematical details that are better covered in several texts [e.g., Bendat and Piersol, 1986] and recent papers [e.g., Brown and Scholz, 1985], the power spectrum is basically the Fourier transform of the profile (or two-dimensional topography). This produces a plot showing power, or variance, as a function of spatial frequency, or scale. These functions are usually plotted as power in $\text{m}^2/\text{cycle}/\text{m}$, or m^3 , vs. spatial wave number ($= \Lambda/2\pi$, where Λ is spatial wavelength). When plotted in log-log coordinates, the functions are approximately linear [e.g., Berry and Hannay, 1978; Farr, 1992], indicating a power-law relationship between roughness and scale. This relationship simplifies the quantitative description of the power spectrum of a profile to two parameters: the slope and offset (y -intercept). Power spectrum slope is a measure of self-similarity related to the fractal dimension, D , by [Brown, 1985]

$$D = \frac{5 + \text{slope}}{2}$$

Power spectrum offset is a measure of overall roughness, sometimes called “roughness amplitude” [Huang and Turcotte, 1989]. For centimeter–meter scales, power spectrum offset has been empirically related to h by [Evans et al., 1992]:

$$h = 40e^{(offset)}$$

Scattering Models

There are two main types of scattering models: facet and Bragg. Facet-type models assume that the roughness is smaller and curvatures larger than λ , so specular scattering dominates from the smooth, tilted facets. The various names for facet-type models include Physical Optics, Geometric Optics, Kirchoff Approximation, Stationary-Phase Approximation, Scalar-Wave Approximation, and the Hagfors Model. In general, these models are most useful at small incidence angles and for smooth surfaces; no cross-polarization terms are predicted.

As an example, the Stationary-Phase Approximation (SPA) is given as [e.g., Kim et al., 1992; Rodríguez et al., 1992]:

$$\sigma_{pp}^0 = \frac{\rho^2 l^2 e^{-(l \tan \theta / 2h)^2}}{4h^2 \cos^4 \theta}$$

where

ρ = Fresnel reflectivity at $\theta = 0$

$$= \left| \frac{1 - \sqrt{\epsilon}}{1 + \sqrt{\epsilon}} \right|^2$$

Note that the SPA gives the same value of σ^0 for both HH and VV polarizations. This is typical of facet-type models since they assume normal reflections from the facets.

The Hagfors Model is better known for its planetary radar applications [e.g., Tyler et al., 1992]:

$$\sigma^0 = \frac{C\rho}{2} \left(\cos^4 \theta + C \sin^2 \theta \right)^{-3/2}$$

where

$C^{-1/2}$ = rms slopes (in radians)

Bragg models are based on Bragg resonance (e.g., X-ray crystallography). These models assume that h and l are smaller than λ , yielding diffuse scattering. Better known Bragg-type models include the Small Perturbation Model and the Muhleman Model. In general, these models are most

useful for large θ and rougher surfaces, including ocean and geologic surfaces; no cross-polarization is predicted for first-order Bragg models. As an example of a Small Perturbation Model (SPM),

$$\sigma_{pp}^0 = 8k^4 h^2 \cos^4 \theta |\alpha_{pp}|^2 W(2k \sin \theta)$$

where

pp = hh or vv polarization

$$k = \lambda / 2\pi$$

$$\alpha_{hh} = \frac{\epsilon - 1}{\left(\cos \theta + \sqrt{\epsilon - \sin^2 \theta} \right)^2}$$

$$\alpha_{vv} = \frac{(\epsilon - 1)(\epsilon + \epsilon \sin^2 \theta - \sin^2 \theta)}{\left(\epsilon \cos \theta + \sqrt{\epsilon - \sin^2 \theta} \right)^2}$$

and W is the power spectrum evaluated at $2k \sin \theta$ only (i.e., the SPM selects only a single scale of roughness, dependent on λ and θ). Note that the ratio of σ_{vv}^0 and σ_{hh}^0 has no roughness dependence and is dependent only on ϵ and θ . Note also that for realistic values of ϵ and θ , σ_{vv}^0 is always larger than σ_{hh}^0 .

Assuming a Gaussian form for the autocorrelation function of the surface, we can reduce W to a function of l [Ulaby et al., 1982]:

$$W(2k \sin \theta) = (l^2 / 2) e^{-(kl \sin \theta)}$$

The Muhleman Model is an empirical model based on the Bragg model, used in planetary radar studies [e.g., Tyler et al., 1992]:

$$\sigma^0 = \frac{\beta \cos \theta}{(\sin \theta + \alpha \cos \theta)^3}$$

α and β are empirical constants, set to 0.111 and 0.0118, respectively, for Magellan SAR data processing (see Chapter 2).

A third type of model seeks to combine the facet and Bragg models; this is the two-scale model, which assumes that a surface can be decomposed into smooth, large-scale facets with small-scale roughness superimposed.

With the development of calibrated radar sensors [van Zyl, 1990] and accurate measurements of centimeter-scale surface roughness [Wall et al., 1991], inversions of some of the models given above have been attempted and validated. Van Zyl et al. [1991] inverted the SPM with three-wavelength (68-, 24-, and 5.5-cm) AIRSAR data to obtain power spectra of lava flow surfaces in the Mojave Desert. They found that varying both λ and θ determined points along the W vs.

$2k \sin \theta$ power spectrum. Varying λ from 68 to 5.5 cm at constant θ (the AIRSAR case) spans a much larger range of $2k \sin \theta$ than does varying θ from typical values of 15 to 50 deg with constant λ (the Magellan SAR case). However, since most natural surfaces seem to have similar power spectrum slopes [Farr, 1992], the single- λ case may still provide significant information on the power spectrum offset (Table 5-1) [Farr, 1992]. It is evident that more work needs to be done on the variability and significance of power spectrum slope.

Table 5-1. Measures of roughness and σ^0 for natural surfaces at Pisgah Lava Field^a

Parameter	Surface		
	Aa	Pahoehoe	Playa
Above (+) or below (-)			
Rayleigh criterion at			
$\theta = 25$ deg ^b	+	+	-
$\theta = 45$ deg ^b	+	+	-
RMS height at 1-cm spacing, cm	39.8	2.97	0.83
Correlation length, cm	110	102	35.6
Power spectrum			
Slope	-1.95	-2.57	-2.34
Offset	-0.55	-2.06	-2.71
σ^0 (25 deg, 5.4 cm, HH), dB	-5.8	-8.5	-11.5
σ^0 (45 deg, 5.4 cm, HH), dB	-6.9	-12.5	-16.5
σ^0 (25 deg, 25 cm, HH), dB	-5.9	-14.0	-20.0
σ^0 (45 deg, 25 cm, HH), dB	-7.9	-18.0	-23.0

^aFrom Arvidson et al., 1993.

^bRayleigh criterion for $\lambda = 12$ cm, $\theta = 25$ deg: 1.6 cm; Rayleigh criterion for $\lambda = 12$ cm, $\theta = 45$ deg: 2.1 cm.

Dielectric Constant (ϵ)

Dielectric constant is a measure of how well electromagnetic waves couple with a material. The relative dielectric constant, ϵ , has a real part, ϵ' , which is the permittivity of the material, and an imaginary part, ϵ'' , called the loss factor. Metals have a very high dielectric constant, approaching infinity for conducting materials. A vacuum has a dielectric constant of 1.0. Most other natural materials have real dielectric constants between 2 and 10 and very small imaginary dielectric constants, between 0.01 and 0.1 [Carmichael, 1982; Ulaby et al., 1982, p. 2081; Ulaby et al., 1990]. Water with dissolved ions, because of its

polarizability, has a dielectric constant much higher, around 80, producing significant effects in radar images of wet areas.

Except for the effect of moisture, the effect of dielectric constant variations on radar images is of secondary importance to surface roughness variations. This is because most natural rocks and soils have dielectric constants that occupy a narrow range of values.

Dielectric constant determines the strength of the Fresnel reflection coefficient in the various scattering models discussed above, and therefore must be understood if quantitative models of radar backscatter are to be constructed. Factors important in the Venusian environment that will affect the dielectric constant are the density of a material and the presence of metals. An empirical relationship has been developed between density, r , and dielectric constant. Ulaby et al. [1990] found that $\epsilon \approx 1.96r$ for a variety of terrestrial rocks.

It has been well established that the highlands of Venus exhibit strong backscatter in radar images and low emissivity in passive radiometer data—characteristics of high dielectric constant material [Pettengill et al., 1988]. Most models at this time favor the presence, either as inclusions or weathering products, of free metals or metallic compounds [Klose et al., 1992]. Since liquid water is not stable on Venus' surface, metals are the only known material that could produce the inferred high dielectric constants.

The loss factor, ϵ'' , determines the strength of absorption of radar waves by the material. For most materials, this factor decreases with wavelength. Dry, well-sorted granular materials are those most easily penetrated by radar waves—to a depth of several wavelengths [Elachi et al., 1984; Farr et al., 1986; Schaber et al., 1986]. On Venus, such granular materials may make up the extended impact-crater-related parabolas [Campbell et al., 1992], wind streaks, and dunes [Greeley et al., 1992].

References

- Arvidson, R. E., M. K. Shepard, E. A. Guinness, S. B. Petrov, J. J. Plaut, D. L. Evans, T. G. Farr, R. Greeley, N. Lancaster, and L. R. Gaddis, 1993, "Characterization of lava-flow degradation in the Pisgah and Cima volcanic fields, California, using Landsat Thematic Mapper and AIRSAR data," *Geol. Soc. Amer. Bull.*, v. 105, p. 175–188.
- Bendat, J. S., and A. G. Piersol, 1986, *Random Data, Analysis and Measurement Procedures*, 2nd ed., New York: John Wiley and Sons, 566 pp.
- Berry, M. V., and J. H. Hannay, 1978, "Topography of random surfaces, comment and reply," *Nature*, v. 273, p. 573.

- Brown, S. R., 1985, "A note on the description of surface roughness using fractal dimension," *Geophys. Res. Lett.*, v. 14, p. 1095–1098.
- Brown, S. R., and C. H. Scholz, 1985, "Broad bandwidth study of the topography of natural rock surfaces," *J. Geophys. Res.*, v. 90, p. 12575–12582.
- Campbell, D. B., N. J. S. Stacy, W. I. Newman, R. E. Arvidson, E. M. Jones, G. S. Musser, A. Y. Roper, and C. Schaller, 1992, "Magellan observations of extended impact crater related features on the surface of Venus," *J. Geophys. Res.*, v. 97, p. 16,249–16,277.
- Carmichael, R. S., 1982, *Handbook of Physical Properties of Rocks, Volume 1*, Florida: CRC Press, 404 pp.
- Elachi, C., L. E. Roth, and G. G. Schaber, 1984, "Spaceborne radar subsurface imaging in hyperarid regions," *IEEE Trans. Geosci. Rem. Sens.*, v. GE-22, p. 383–388.
- Elachi, C., 1988, *Spaceborne Radar Remote Sensing: Applications and Techniques*, New York: IEEE Press, 254 pp.
- Evans, D. L., T. G. Farr, and J. J. van Zyl, 1992, "Estimates of surface roughness derived from synthetic aperture radar (SAR) data," *IEEE Trans. Geosci. Rem. Sens.*, v. 30, p. 382–389.
- Farr, T. G., C. Elachi, Ph. Hartl, and K. Chowdhury, 1986, "Microwave penetration and attenuation in desert soil: A field experiment with the Shuttle Imaging Radar," *IEEE Trans. Geosci. Rem. Sens.*, v. GE-24, p. 590–594.
- Farr, T. G., 1992, "Microtopographic evolution of lava flows at Cima volcanic field, Mojave Desert, California," *J. Geophys. Res.*, v. 97, p. 15171–15179.
- Ford, J. P., et al., 1989, *Spaceborne Radar Observations: A Guide for Magellan Radar-Image Analysis*, Publication 89-41, Jet Propulsion Laboratory, Pasadena, California, 126 p.
- Fung, A. K., and G. W. Pan, 1987, "A scattering model for perfectly conducting random surfaces: I. Model development," *Int. J. Remote Sens.*, v. 8, p. 1579–1593.
- Greeley, R., R. E. Arvidson, C. Elachi, M. A. Geringer, J. J. Plaut, R. S. Saunders, G. Schubert, E. R. Stofan, E. J. P. Thouvenot, S. D. Wall, and C. M. Weitz, 1992, "Aeolian features on Venus: Preliminary Magellan results," *J. Geophys. Res.*, v. 97, p. 13,319–13,345.
- Huang, J., and D. L. Turcotte, 1989, "Fractal mapping of digitized images: Application to the topography of Arizona and comparisons with synthetic images," *J. Geophys. Res.*, v. 94, p. 7491–7495.
- Kim, Y., E. Rodríguez, and S. L. Durden, 1992, "A numerical assessment of rough surface scattering theories: Vertical polarization," *Radio Sci.*, v. 27, p. 515–527.
- Klose, K. B., J. A. Wood, and A. Hashimoto, 1992, "Mineral equilibria and the high radar reflectivity of Venus mountaintops," *J. Geophys. Res.*, v. 97, p. 16,353–16,369.
- Peake, W. H., and T. L. Oliver, 1971, *The Response of Terrestrial Surfaces at Microwave Frequencies*, Columbus, Ohio: Ohio State University, Electroscience Laboratory, 2440-7, Technical Report AFAL-TR-70-301.
- Pettengill, G. H., P. G. Ford, and G. D. Chapman, 1988, "Venus: Surface electromagnetic properties," *J. Geophys. Res.*, v. 93, p. 14,881–14,892.
- Rodríguez, E., and Y. Kim, 1992, "A unified perturbation expansion for surface scattering," *Radio Sci.*, v. 27, p. 79–93.
- Rodríguez, E., Y. Kim, and S. L. Durden, 1992, "A numerical assessment of rough surface scattering theories: Horizontal polarization," *Radio Sci.*, v. 27, p. 497–513.
- Schaber, G. G., G. L. Berlin, and W. E. Brown, 1976, "Variations in surface roughness within Death Valley, California: geologic evaluation of 25-cm-wavelength radar images," *Geol. Soc. Am. Bull.*, v. 87, p. 29–41.
- Schaber, G. G., J. F. McCauley, C. S. Breed, and G. R. Olhoeft, 1986, "Shuttle imaging radar: Physical controls on signal penetration and subsurface scattering in the eastern Sahara," *IEEE Trans. Geosci. Rem. Sens.*, v. GE-24, p. 603–623.
- Tyler, G. L., R. A. Simpson, M. J. Maurer, and E. Holmann, 1992, "Scattering properties of the Venusian surface: Preliminary results from Magellan," *J. Geophys. Res.*, v. 97, p. 13,115–13,139.
- Ulaby, F. T., R. K. Moore, and A. K. Fung, 1982, *Microwave Remote Sensing, Volumes 1, 2, and 3*, Massachusetts: Addison-Wesley, 2162 pp.
- Ulaby, F. T., T. H. Bengal, M. C. Dobson, J. R. East, J. B. Garvin, D. L. Evans, 1990, "Microwave dielectric properties of dry rocks," *IEEE Trans. Geosci. Rem. Sens.*, v. 28, p. 325–336.
- van Zyl, J. J., 1990, "A technique to calibrate polarimetric radar images using only image parameters and trihedral corner reflectors," *IEEE Trans. Geosci. Rem. Sens.*, v. GE-28, p. 337–348.
- van Zyl, J. J., C. F. Burnette, and T. G. Farr, 1991, "Inference of surface power spectra from inversion of multifrequency polarimetric radar data," *Geophys. Res. Lett.*, v. 18, p. 1787–1790.
- Wall, S. D., T. G. Farr, J.-P. Muller, P. Lewis, and F. W. Leberl, 1991, "Measurement of surface microtopography," *Photogramm. Eng. Rem. Sens.*, v. 57, p. 1075–1078.